Ceramics International 44 (2018) 14113–14121

Contents lists available at ScienceDirect

Ceramics International

journal homepage: www.elsevier.com/locate/ceramint

Effect of Zn addition on the structure and electrochemical properties of co-doped $BaCe_{0.6}Zr_{0.2}Ln_{0.2}O_{3-\delta}$ (Ln = Y, Gd, Yb) proton conductors

Javier Zamudio-García[a], Jose M. Porras-Vázquez[a,*], Lucía dos Santos-Gómez[a], Enrique R. Losilla[a], David Marrero-López[b]

[a] Universidad de Málaga, Dpto. de Química Inorgánica, Cristalografía y Mineralogía, 29071 Málaga, Spain
[b] Universidad de Málaga, Dpto. de Física Aplicada I, Laboratorio de Materiales y Superficies, 29071 Málaga, Spain

ARTICLE INFO

Keywords:
Barium cerate
Barium zirconate
Proton conductor
SOCs
Sintering aid

ABSTRACT

In this work, $BaCe_{0.6}Zr_{0.2}Y_{0.2-x}Yb_xO_{3-\delta}$ and $BaCe_{0.6}Zr_{0.2}Gd_{0.2-x}Yb_xO_{3-\delta}$ (x = 0–0.20), proton conducting materials are prepared by the freeze-drying precursor method. The sintering conditions were optimized by adding Zn $(NO_3)_2{\cdot}6H_2O$ as sintering additive. The materials are thoroughly characterized by different structural and microstructural techniques, including X-ray diffraction, scanning and transmission electron microscopy, and thermogravimetric-differential thermal analysis. The addition of Zn favours the phase formation and densification at lower sintering temperatures; however, it leads to the segregation of a Zn-rich secondary phase, with general formula $BaLn_2ZnO_5$ (Ln=Y, Gd and Yb), which is identified and quantified for the first time. All samples with Zn as sintering aid exhibit cubic structure; however, the samples without Zn crystallize with orthorhombic or cubic structure, depending on the composition and thermal treatment. The electrical properties are studied by impedance spectroscopy. A deep analysis of the bulk and grain boundary contributions to the conductivity has revealed that the bulk conductivity remains almost unchanged along both series over Yb-doping; however, the grain boundary resistance decreases. The highest conductivity values are found for the intermediate members of both series, $BaCe_{0.6}Zr_{0.2}Y_{0.1}Yb_{0.1}O_{3-\delta}$ and $BaCe_{0.6}Zr_{0.2}Gd_{0.1}Yb_1O_{3-\delta}$, with 33 and 28 mS cm^{-1} at 750 °C, respectively.

1. Introduction

Solid oxide fuel cells and electrolysis cells are efficient devices that produce energy and hydrogen gas, respectively. They are formed by two porous ceramic electrodes separated by a dense electrolyte, which could be an oxide-ion or proton conducting material. In particular, proton conducting solid oxide cells (PC-SOC) have the advantage to operate at lower temperatures than the traditional oxide ion conducting cells (400–700 °C), due to the fact that the proton mobility is higher than the oxide ions at intermediate temperatures. The reduction of the operating temperature has several benefits, such as reduction of compatibility issues and longer durability of the cells components.

Most of the electrolytes for PC-SOCs are based on perovskite-type materials, such as $BaCeO_3$ and $BaZrO_3$. The highest conductivities are observed for doped-$BaCeO_3$, ~0.01 S cm^{-1} at 600 °C; unfortunately, they have poor chemical stability in the presence of CO_2. On the contrary, $BaZrO_3$-based electrolytes exhibit improved stability in CO_2 and H_2O environments; however, extremely high sintering temperatures, as high as 1700 °C, are necessary to achieve densification, which is unsuitable from an industrial point of view. Therefore, a compromise solution has been proposed by preparing compounds containing both cerium and zirconium, combining the conductivity and stability properties of cerates and zirconates, respectively. [1–6]. In order to increase the conductivity, $BaCe_{1-x-y}Zr_xLn_yO_{3-\delta}$ (BCZ) materials are doped with trivalent cations, such as Ln = Y^{3+}, Nd^{3+}, Sm^{3+}, Gd^{3+}, Yb^{3+}, Tb^{3+} and Dy^{3+} [5,7–20]. In general, Y^{3+} is the most widely used alliovalent dopant for both $BaCeO_3$ and $BaZrO_3$ electrolytes. However, the highest values of proton conductivity in $BaCeO_3$ series have been reported for Gd-doping, because this substitution produces a smaller lattice distortion of the cell with a higher free volume for oxygen diffusion [20,21].

Co-doping with alliovalent elements is an alternative strategy to improve the properties of $Ba(Ce,Zr)O_3$ based electrolytes. For instance, Yang et al. have studied the effect of Y and Yb co-doping in $BaCe_{0.7}Zr_{0.1}Y_{0.2-x}Yb_xO_{3-\delta}$ ($0 \le x \le 0.2$) series [22]. The maximum conductivity value, about 60 mS cm^{-1} at 750 °C, was found for x = 0.1. In addition, these materials showed high tolerance to sulphur and

* Corresponding author. Present address: Dpto. de Química Inorgánica, Cristalografía y Mineralogía, Facultad de Ciencias, Campus de Teatinos, Universidad de Málaga, 29071 Málaga, Spain.
E-mail address: josema@uma.es (J.M. Porras-Vázquez).

https://doi.org/10.1016/j.ceramint.2018.05.010
Received 19 April 2018; Received in revised form 2 May 2018; Accepted 2 May 2018
Available online 03 May 2018

coking poisoning, due to an improvement of the catalytic activity towards sulphur oxidation and hydrocarbon cracking and reforming.

Different synthetic methods have been used to improve the properties of $BaCe_{0.7}Zr_{0.1}Y_{0.1}Yb_{0.1}O_{3-\delta}$, such the Pechini method [23,24], attrition milling [11], coprecipitation [25], direct current sintering [26], and atmospheric plasma spray [27]. However, sintering temperatures above 1500 °C are still necessary to achieve densification of these materials, but lead to BaO evaporation and the segregation of CeO_2 [28]. In order to reduce the temperatures, transition metals, such as Co, Fe, Ni and Zn, have been used as sintering aids [29–34]. Among them, Zn^{2+} has shown to be the most effective because allows reducing the sintering temperature to 1000–1200 °C without altering significantly the transport properties of the parent compound [32–35]. However, the addition of Zn leads to the segregation of minor secondary phases, which are still unidentified. Moreover, the origin of these impurities and how to avoid their formation is still unclear.

In this work, a co-doping strategy with Y^{3+}, Yb^{3+} and Gd^{3+} was employed to obtain two series of compounds $BaCe_{0.6}Zr_{0.2}Y_{0.2-x}Yb_xO_{3-\delta}$ and $BaCe_{0.6}Zr_{0.2}Gd_{0.2-x}Yb_xO_{3-\delta}$ ($0 \le x \le 0.2$). The materials are synthesized by both solid state reactive sintering and freeze-drying precursors. Dense ceramic pellets without and with Zn addition are prepared, and the structural and electrical properties are investigated by X-ray diffraction, scanning and transmission electron microscopy and impedance spectroscopy.

2. Experimental

2.1. Synthesis and sintering conditions

Materials with composition $BaCe_{0.6}Zr_{0.2}Y_{0.2-x}Yb_xO_{3-\delta}$ and $BaCe_{0.6}Zr_{0.2}Gd_{0.2-x}Yb_xO_{3-\delta}$ (x = 0, 0.05, 0.10, 0.15 and 0.20) were prepared by a freeze-drying precursor method (FD) from: $Ba(NO_3)_2$, $Ce(NO_3)_3{\cdot}6H_2O$, $ZrO(NO_3)_2{\cdot}6H_2O$, $Y(NO_3)_3{\cdot}6H_2O$, $Gd(NO_3)_3{\cdot}6H_2O$ and $Yb(NO_3)_3{\cdot}5H_2O$ (Sigma-Aldrich, purity > 99%). The precursor solutions were obtained by dissolving the different reagents in water. An ethylenediaminetetraacetic acid (EDTA) solution was added as a complexing agent in a 1:1 ligand: metal molar ratio. The solutions were frozen in liquid nitrogen, followed by dehydration by vacuum sublimation in a Scanvac Coolsafe freeze-dryer. Further experimental details on the freeze-drying process are given elsewhere [20,31]. The amorphous precursor powders were initially calcined at 300 °C for 1 h to prevent rehydration, at 800 °C for 1 h to eliminate carbonaceous species, and subsequently at 1100 °C for 1 h to obtain the crystalline materials. The resulting powders were reground for 2 h at 200 rpm in a Fritsch ball mill (model Pulverisette 7, zirconia balls and vessel) without and with 4 mol% of $Zn(NO_3)_2{\cdot}6H_2O$ (1 wt% ZnO) as sintering aid in absolute ethanol media. It has to be commented that this is the optimum Zn-content to obtain dense ceramics without altering significantly their transport properties [31,36]. The powders were pressed into pellets at 500 MPa (10 mm diameter and 1 mm of thickness) and sintered at 1500 °C for 1 h for samples without Zn and 1200 °C for 15 min, 5 and 10 h for samples with Zn. The pellets were slowly cooled to room temperature at 5 °C min^{-1} and finely ground into powders before further characterization. Hereafter, the series of compounds $BaCe_{0.6}Zr_{0.2}Y_{0.2-x}Yb_xO_{3-\delta}$ and $BaCe_{0.6}Zr_{0.2}Gd_{0.2-x}Yb_xO_{3-\delta}$ are labelled as YYb_x and $GdYb_x$, respectively, where x represents the ytterbium content.

For the sake of comparison, some of these materials were prepared by reactive sintering method (SSR) to compare their properties with those obtained by freeze-drying precursors. For this purpose, the reagents: $BaCO_3$, ZrO_2, CeO_2 and Ln_2O_3 (Ln=Y, Gd, Yb) (Sigma-Aldrich, purity > 99%) were mixed in the ball mill in absolute ethanol media and then dried in a muffle furnace. The resulting powder mixture was pressed into pellets and sintered at 1500 °C for 5 h. Several regrinding and thermal treatments were used to achieve single phase materials. The relative density of the pellets was lower than 85% so that they were structurally characterized but not electrically analyzed.

2.2. Structural and thermal characterization

All compounds were analyzed by laboratory X-ray powder diffraction (XRPD) at room temperature. The patterns were collected on a PANalytical Empyrean with CuK_α radiation. The overall measurement time was approximately 4 h per pattern over the 10–70° (2θ) angular range, with a 0.017° step size. Phase identification and structural analysis were performed with X'Pert HighScore Plus and the GSAS suite programs, respectively [37,38].

Thermogravimetric analysis (TGA) data were recorded on a SDT-Q600 analyzer (TA Instruments) under wet (~ 2 vol% H_2O) air at a heating/cooling rate of 5 °C min^{-1} from room temperature to 950 °C. Two heating and cooling cycles were performed to test the reproducibility of the measurements.

2.3. Microstructural and electrical characterization

The microstructure of the ceramics was observed by scanning electron microscopy (SEM) (Jeol JSM-6490LV). Grain size of the dense pellets was estimated from the SEM micrographs, using the linear intercept method [39]. Energy dispersive spectroscopy (EDS) and selected area electron diffraction (SAED) were performed with a high angle annular dark-field scanning transmission electron microscopy (HAADF-STEM) (FEI, Talos F200X).

For the electrical characterization, platinum ink (METALOR® 6082) was coated on both sides of the pellets, followed by heating at 750 °C for 1 h in air to form the electrodes. Impedance spectra were acquired using a frequency response analyzer (Solartron 1260) in dry and wet air (2 vol%. of H_2O, bubbling through water at room temperature). The spectra were recorded on the cooling process from 750 to 100°C with a stabilization time of 30 min between consecutive measurements. The resistance and capacitance values of the different processes were deconvoluted by fitting the data with equivalent circuit models using the ZView program [40].

3. Results and discussion

3.1. Single phase formation and optimization of the synthesis temperature

XRPD patterns of a representative sample with composition $YYb_{0.1}$, prepared by freeze-drying precursors and calcined at different temperatures, are shown in Fig. 1. Different compounds are identified after calcining the precursor powders at 800 °C, including a $Ba(Ce,Zr)O_{3-\delta}$ (BCZ) perovskite-related phase, and impurities of $BaCO_3$ (PDF 00-001-0506) and CeO_2 (PDF 00-001-0800). At 1100 °C the main phase is the BCZ perovskite, with a very small amount of unreacted $BaCO_3$. Finally, pure compounds are obtained after calcining at 1500 °C for 1 h. Fig. S1 (Supplementary information) displays the XRPD patterns of the remaining members of YYb_x and $GdYb_x$ series at 1500 °C. No secondary phases are detected for all compositions; however, the patterns show a different degree of peak splitting, depending on the phase composition, indicating that the samples crystallize with different symmetry, either cubic or orthorhombic.

Fig. 1 also compared XRPD patterns of $YYb_{0.1}$ prepared without and with Zn. The sample without Zn shows peak splitting due to the orthorhombic distortion of the unit cell, as it was mentioned before; however, the sample containing Zn as sintering aid crystallizes with a cubic structure.

The same materials were prepared by solid state reactive sintering under similar experimental conditions at 1500 °C for 10 h. In this case, the peak splitting is more important, indicating a less symmetric unit cell of the materials. Moreover, the lattice distortion decreases when the materials are milled, homogenized, and calcined again at 1500 °C (Fig. S2). This indicates that the cation composition in the bulk material

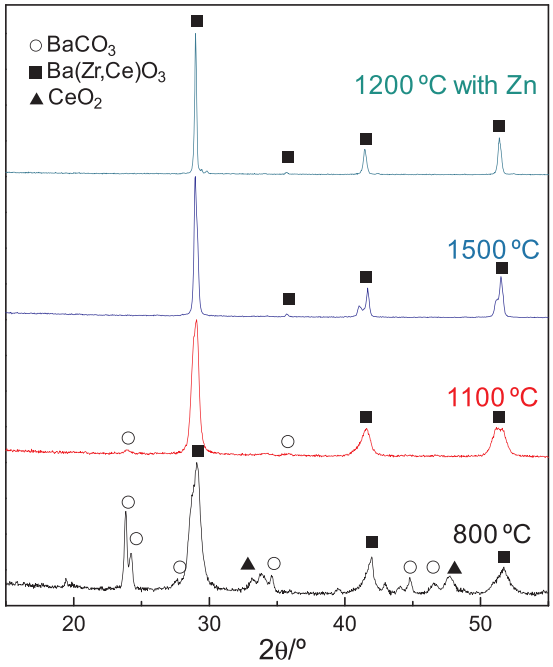

Fig. 1. XRPD patterns of $BaCe_{0.6}Zr_{0.2}Y_{0.1}Yb_{0.1}O_{3-\delta}$ powders obtained by the freeze-drying method and calcined at different temperatures.

is not homogeneously distributed when the compounds are synthesized in only one step through the ceramic method, modifying the crystal symmetry of the materials. Amsif et al. observed a similar behaviour in $BaCe_{0.9-x}Zr_xY_{0.1}O_{3-d}$ ($0 \leq x \leq 1$) series, XRPD patterns showed very asymmetric diffraction peaks, which were associated with the presence of different perovskite type compounds with similar cell parameters [31]. It is well reported that the crystal structure of $BaCe_{1-x}Zr_xO_{3-\delta}$ materials depends on the composition, the ionic radii of the trivalent dopant and other factors, such as the synthesis method and calcination temperature employed. For example, Shi et al. reported an orthorhombic structure for $BaCe_{0.5}Zr_{0.3}Y_{0.2-x}Yb_xO_{3-\delta}$ prepared by citric acid-nitrate gel combustion process followed by sintering at 1550 °C [41]. Malavasi et al. have studied the $BaCe_{0.85-x}Zr_xY_{0.15}O_{3-\delta}$ ($0.1 < x < 0.4$) series by combined neutron and synchrotron X-ray diffraction, and four different crystal structures were found for the samples with $x < 0.2$ between room temperature and 800 °C. For higher Zr-doping levels ($x = 0.3$ and 0.4), the samples showed a more symmetric rhombohedral structure at room temperature [42]. In contrast, Lyagaeva et al. reported a cubic structure for $BaCe_{0.5}Zr_{0.3}Y_{0.2-x}Yb_xO_{3-\delta}$ series [43].

The samples with Zn-addition, sintered at 1200 °C for 5 h, exhibit better crystallinity and no splitting of the diffraction peaks is observed compared to the samples without Zn, which indicates a cubic symmetry of the crystal lattice (Fig. 2). The same trend is observed for all members of both YYb_x and $GdYb_x$ series. In addition, diffraction peaks ascribed to $Zn(NO_3)_2{\cdot}6H_2O$ addition are not detected; however, small peaks are observed at 30°, due to the segregation of a Zn-rich phase, $BaLn_2ZnO_5$ (Ln=Y, Gd and Yb) (PDF 01-089-8283 and 01-089-8280) (inset Fig. 2). It has to be noted that no rhombohedral polymorphs were detected for any member of the series.

To gain further insights on the formation of these minor secondary phases, different pellets of $GdYb_{0.1}$ with 4 mol% of Zn were sintered at 1200 °C for 15 min, 5 and 10 h (Fig. S3). All samples showed relative densities above 95%, independently of the sintering time, and the corresponding XRPD patterns showed that the amount of $BaGd_2ZnO_5$ secondary phase increases for longer sintering times (inset Fig. S3). However, preliminary impedance spectroscopy studies were carried out showing that best results were obtained for the samples heated for 5 h (Fig. S4). Lower sintering times led to a significance worsening of the electrical properties and longer ones resulted in no improvement, therefore, sintering times of 5 h were chosen as the optimal synthesis-sintering conditions.

In order to check the cation homogeneity of the samples, the sintered pellets were analyzed by HAADF-STEM. Fig. 3 shows the EDS results for a sample with composition $GdYb_{0.1}$ prepared with Zn at 1200 °C for 5 h. Notice that Zn is not detected in the grains of the ceramic pellets; however, small grains are enriched in Zn, Ba and the trivalent dopant. This finding confirms that the reaction product observed by XRPD is $BaGd_2ZnO_5$ (PDF 01-089-8280), with an orthorhombic symmetry.

Fig. 4a shows a HRTEM image for $GdYb_{0.1}$ near the grain boundary regions. Notice that secondary phases or amorphous phase segregations are not detected in this region, contrary to previous studies for BZY samples with Cu and Li additives [44,45]. An amorphous and thick grain boundary layer of 10 nm was observed for Cu-BZY and somewhat thinner for Li-BZY. In this last case, the amorphous layer was associated with the formation of an amorphous Li–Y–O glass.

On the other hand, SAEDs are correctly indexed by considering a cubic unit cell with a lattice parameter of 4.3 Å, confirming the cubic symmetry observed by the XRPD studies (Fig. 4b and c).

3.2. Structural characterization

XRPD patterns for both series of compounds were analyzed by the Rietveld method in a cubic (s.g. *Pm-3m*) or orthorhombic structure (s.g. *Pbnm)*, depending on the material composition and synthetic conditions used (Tables S1 and S2). During the analysis the occupancy factors were conveniently fitted to the proposed stoichiometry and the usual parameters were refined: background, zero, histogram scale factor and peak shape coefficients.

Representative Rietveld plots are shown in Fig. 5 for $YYb_{0.1}$ and $GdYb_{0.1}$ samples obtained by reactive sintering and freeze-drying precursors with and without Zn. All remaining samples showed similar fits and agreement factors were good. As can be seen, the refinements are satisfactory and all diffraction peaks are indexed, including the small peaks attributed to $BaLn_2ZnO_5$ (Ln=Y, Gd and Yb), refined in an orthorhombic cell (ICSD files 35591 and 88602) (Table S2). These secondary phases were quantified and resulted in a 2–4 wt% of $BaLn_2ZnO_5$ (2–3 mol% Zn), indicating that most of the sintering aid is segregated to $BaLn_2ZnO_5$ and not incorporated into the main perovskite phase, in agreement with the HAADF-STEM analysis. It is worth mentioning that to the best of our knowledge, this is the first time that this secondary phase is reported and quantified.

Regarding YYb_x series, samples prepared by reactive sintering and by freeze-drying without Zn addition, always crystallize in an orthorhombic symmetry (Fig. 5a–c). In contrast, $GdYb_x$ compounds with $x \leq 0.1$ present a cubic structure, independent on the synthetic method employed (Fig. 5d–f). Higher ytterbium contents for $GdYb_x$ lead to an orthorhombic symmetry. On the other hand, all members of YYb_x and $GdYb_x$ series crystallize with a cubic symmetry after Zn addition and sintering at 1200 °C.

Unit cell parameters and agreement factors are shown as Supplementary information in Table S1 and S2 for the samples prepared by the freeze-drying method. Cell parameters within the series decrease as Yb-doping increases due to the smaller ionic radii of Yb^{3+} (0.868 Å) compared to those of Y^{3+} (0.9 Å) and Gd^{3+} (0.938 Å), all of them in an octahedral coordination. Moreover, the cells parameters of YYb_x series are always lower than those of $GdYb_x$ series. This is the expected trend considering the smaller size of Y^{3+} compared to that of Gd^{3+}.

Samples sintered with Zn at 1200 °C exhibit somewhat larger unit cell volume when compared to the same materials without Zn. This behaviour might be attributed to several factors, including minor incorporation of the Zn^{2+} into the perovskite structure and the formation of a reaction product containing the Ba, Zn and the trivalent dopant, as it was mentioned above. This leads to a variation of the dopant

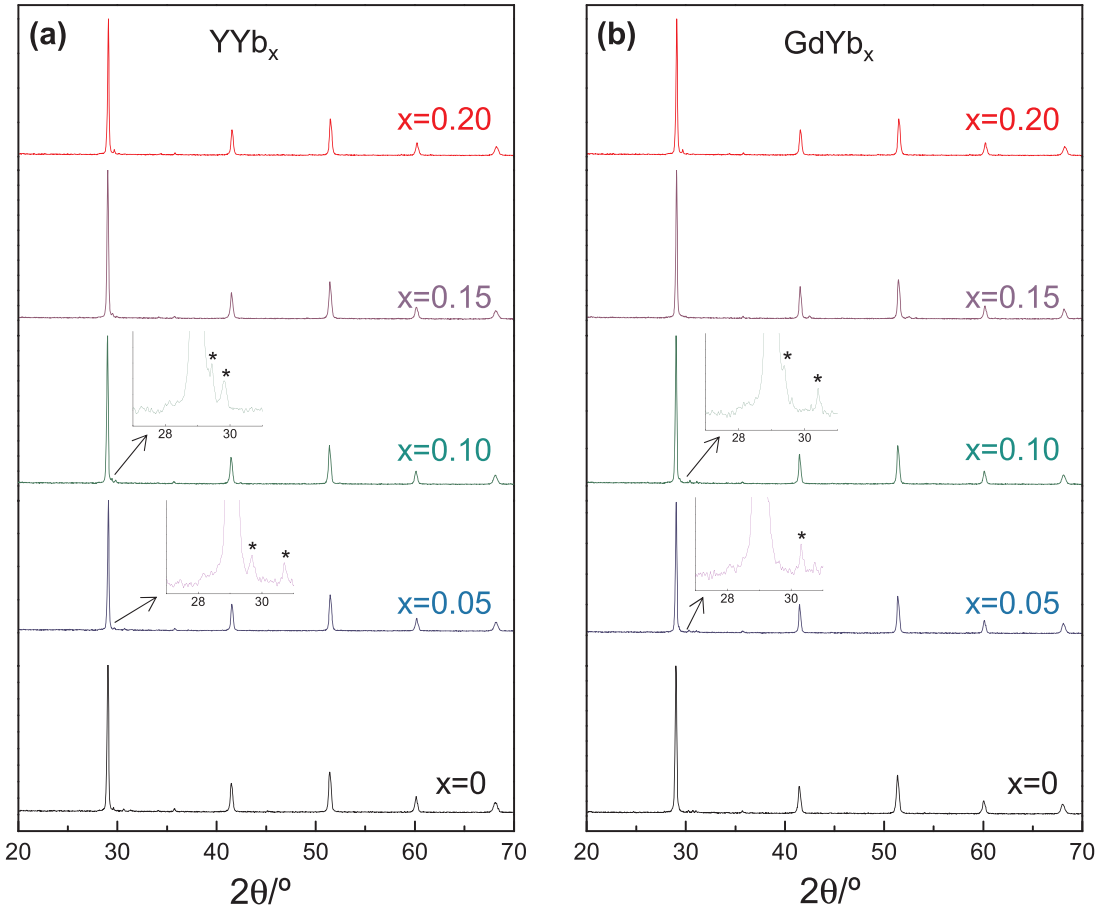

Fig. 2. XRPD patterns of (a) $BaCe_{0.6}Zr_{0.2}Y_{0.2-x}Yb_xO_{3-\delta}$ (YYb_x) and (b) $BaCe_{0.6}Zr_{0.2}Gd_{0.2-x}Yb_xO_{3-\delta}$ ($GdYb_x$) series with 4mol% of Zn heated at 1200 °C for 5 h.

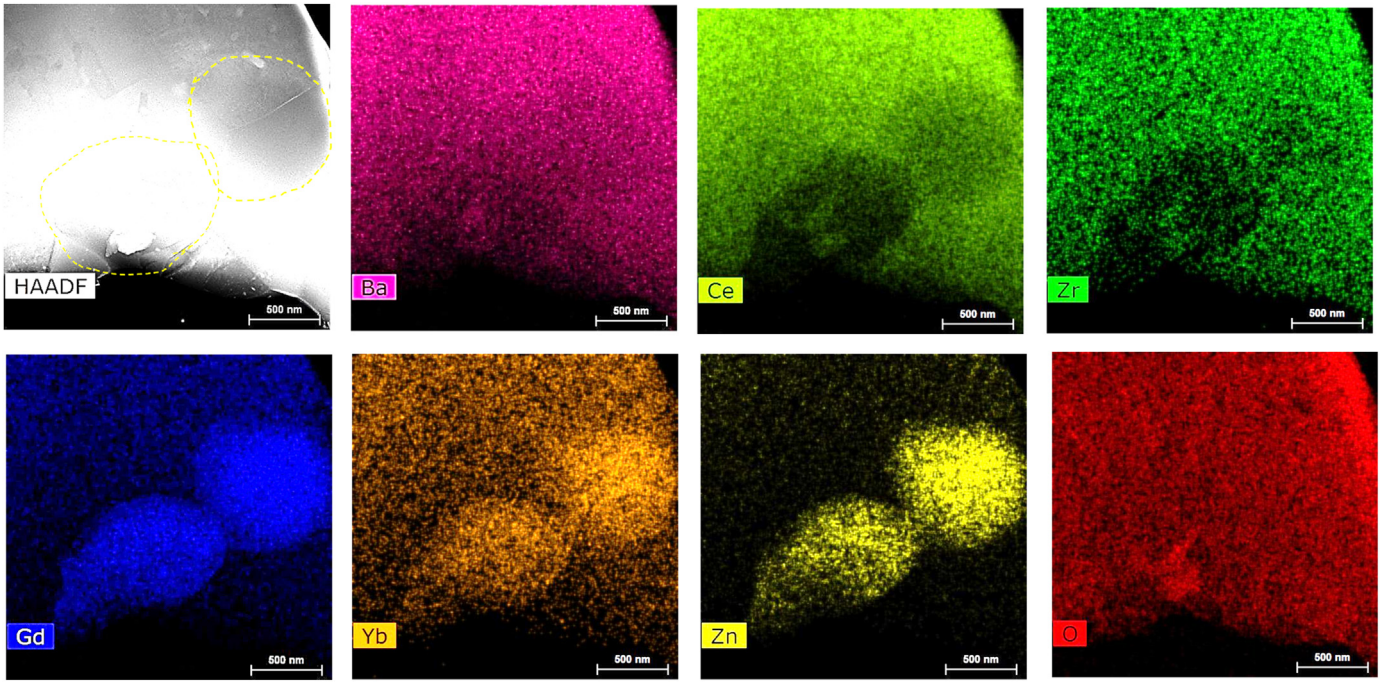

Fig. 3. STEM-HAADF image and EDS mappings of $BaCe_{0.6}Zr_{0.2}Gd_{0.1}Yb_{0.1}O_{3-\delta}$ with 4 mol% of Zn sintered at 1200 °C for 5 h.

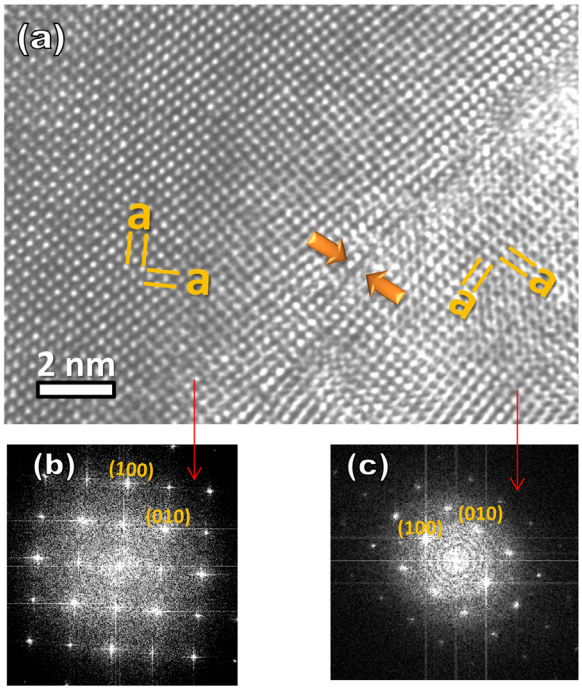

Fig. 4. (a) HRTEM of $BaCe_{0.6}Zr_{0.2}Gd_{0.1}Yb_{0.1}O_{3-\delta}$ with 4 mol% of Zn and sintered at 1200 °C for 5 h, showing a grain boundary without the presence of phase segregations. The SAED images (b) and (c) confirm the cubic structure of the material.

concentration in the structure and an increase of the unit cell volume.

3.3. Thermal analysis

The concentration of oxygen vacancies available for hydration in the structure was estimated by thermogravimetric analysis as a function of the temperature. The heating and cooling curves were reproducible in two different thermal cycles and, for simplicity, only the last cooling curve is shown in Fig. S5. As can be seen, all samples show the typical behaviour of a proton conductor, where a weight increase takes place on cooling at about 700 °C, due to the exothermic incorporation of water into the oxide vacancies, according to the following equation:

$$H_2O(g) + O_O^x + v_O^{\bullet\bullet} \rightarrow 2OH_O^{\bullet} \quad (1)$$

The number of water molecules per mole of compound is determined and its relationship with the Yb content is showed in Fig. S5c. It can be seen that the water adsorption increases with Yb-doping, in agreement with the results published by Yang et al. [22], where the co-doping leads to and enhancement of the water adsorption capabilities. The lower water contents are observed for the parent compounds, i.e. 0.075 and 0.077 mol H_2O/moles of compound for YYb_0 and $GdYb_0$, respectively. Conversely, the highest water adsorption was observed for $Yb_{0.2}$, with 0.093 mol H_2O/moles of compound. For intermediate Yb content, $GdYb_{0.1}$ exhibits somewhat higher water uptake than $YYb_{0.1}$, 0.091 and 0.088 mol H_2O/moles of compound, respectively, indicating that the Gd-containing samples present, in general, higher proton concentration than Y-containing samples.

It is important to mention that the total amount of oxygen vacancies for all samples is the same and therefore the water uptake is expected to be similar. However, it has been reported through neutron powder diffraction and water uptake studies that the amount of water adsorption is dependent on the crystal structure [46]. Therefore, in our work, the small differences in water uptake might be ascribed to the different symmetry of the samples. In order to confirm this point, synchrotron X-ray and neutron powder diffraction studies are necessary.

3.4. Microstructural characterization

Typical SEM micrographs for $GdYb_x$ series without Zn addition and sintered at 1500 °C for 5 h are shown in Fig. 6. All samples exhibit

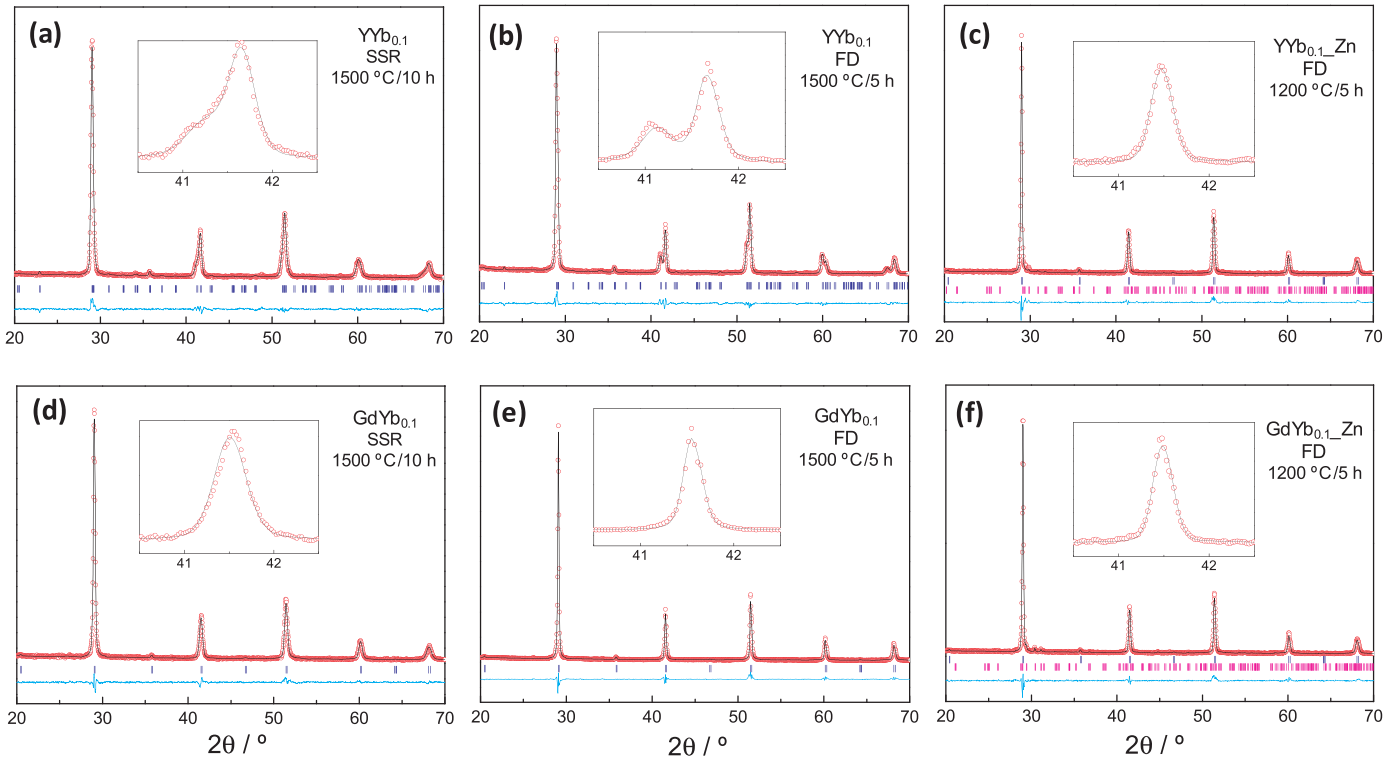

Fig. 5. Rietveld plots of $BaCe_{0.6}Zr_{0.2}Y_{0.1}Yb_{0.1}O_{3-\delta}$ and $BaCe_{0.6}Zr_{0.2}Gd_{0.1}Yb_{0.1}O_{3-\delta}$ samples prepared by solid state reactive sintering (SSR) (a, d) and freeze-drying precursors (FD) without (b, e) and with Zn addition (c, f). In plots (c, f), Bragg marks correspond to the main perovskite phase and $BaLn_2ZnO_5$ (Ln=Y, Gd and Yb).

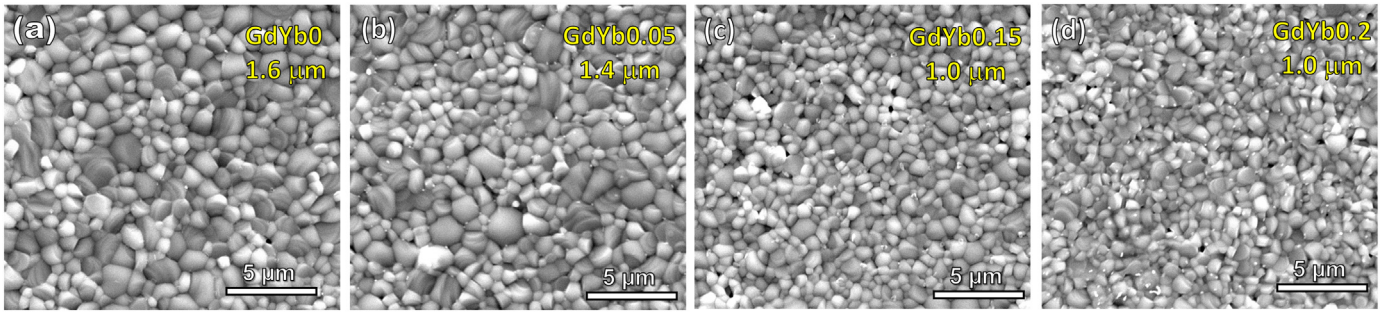

Fig. 6. SEM micrographs of the surface of the $BaCe_{0.6}Zr_{0.2}Gd_{0.2-x}Yb_xO_{3-\delta}$ series sintered at 1500 °C for 1 h without Zn addition.

relative density above 95%. The main microstructural difference between the samples is the average grain size, which decreases as Yb-doping increases, from 1.6 µm for $GdYb_0$ to 1.0 µm for $Yb_{0.2}$. In general, the densification and the grain growth in ceramic materials are controlled by grain boundary diffusion rather than bulk diffusion. The different segregation level of the dopant at the grain boundary reduces the cation mobility at this region during the sintering process, and consequently, the grain growth rate decreases. In this case, the grain growth depends on several factors, such as dopant type and content. For instance, the grain size in doped-$BaCe_{0.9}Ln_{0.1}O_{3-\delta}$ decreases nearly linearly with the ionic radii of the dopant La > Nd > Sm > Gd > Yb [20]. A similar behaviour is observed here for $GdYb_x$, the ceramic grain size decreases as Yb-doping increases due to the smaller ionic radii of Yb in comparison to Gd (Fig. 6). An analogous trend is seen for related materials, such as doped CeO_2 and doped ZrO_2 [47].

The addition of 4 mol% of Zn improves the densification of the ceramics at lower sintering temperature. Dense pellets with relative density above 95% are obtained after sintering at 1200 °C for 15 min and 5 h (Fig. 7). Although the samples sintered for a short time (< 5 h) are dense, the grain size is very irregular and it cannot be determined. Large grains formed by aggregate of particles are observed (Fig. 7a), indicating that the sintering process is not completed. Ceramics sintered at 1200 °C for 5 h show a large grain size, e.g. 4.6 µm for $GdYb_{0.1}$ compared to 1.2 µm for the same sample without Zn and sintered at 1500 °C. The same behaviour is observed for the YYb_x series.

These results clearly indicate that Zn has two different effects on the densification of BCZ electrolytes; it improves the densification but also enhances the grain size growth at lower temperature. This possibly has important effects on the electrical properties since the conductivity of BCZ electrolytes is negatively influenced by the high grain boundary resistance.

3.5. Electrical characterization

The samples were studied by impedance spectroscopy in wet air (2 vol% water). Only the results for those samples with Zn addition and sintered at 1200 °C for 5 h are compared, since these are prepared at reduced temperature and consequently they are more interesting for practical applications. In addition, previous studies demonstrate that the Zn-addition has no ill effects on the transport properties of $BaCe_{0.9-x}Zr_xY_{0.1}O_{3-\delta}$ system [31,33].

Impedance spectra show similar features for all samples. At low temperature, three different contributions assigned to the bulk, grain

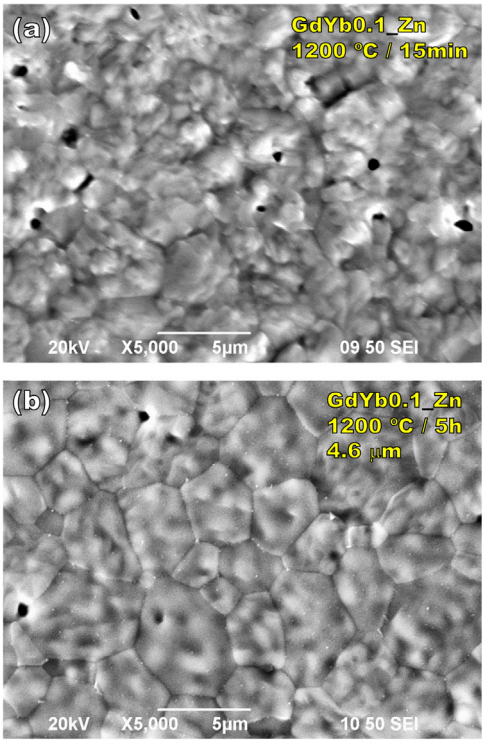

Fig. 7. SEM micrographs of the $BaCe_{0.6}Zr_{0.2}Gd_{0.1}Yb_{0.1}O_{3-\delta}$ surface sintered at 1200 °C for 15 min and 5 h with 4 mol% of Zn.

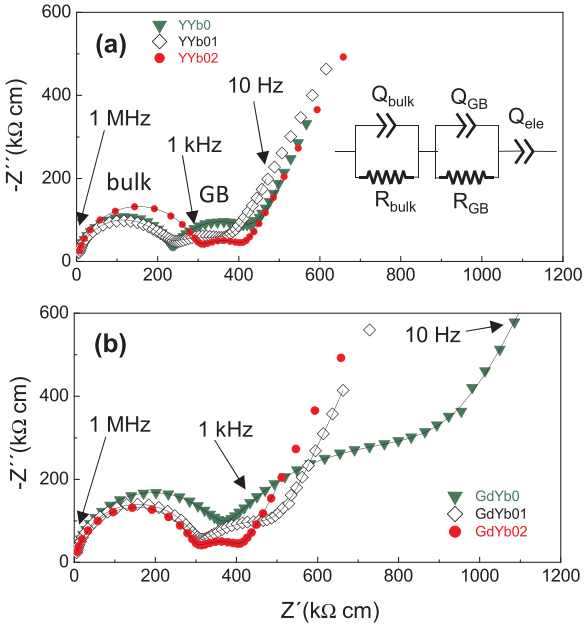

Fig. 8. Representative impedance spectra of a) $BaCe_{0.6}Zr_{0.2}Y_{0.2-x}Yb_xO_{3-\delta}$ and b) $BaCe_{0.6}Zr_{0.2}Gd_{0.2-x}Yb_xO_{3-\delta}$ pellets at 100 °C; sintered at 1200 °C for 5 h with Zn as sintering aid. The inset of (a) shows the equivalent circuit used to analyse the impedance spectra, where the subscripts *b*, *gb* and *e* denote the bulk, the grain boundary and electrode processes, respectively. The solid lines correspond to the fitting curves.

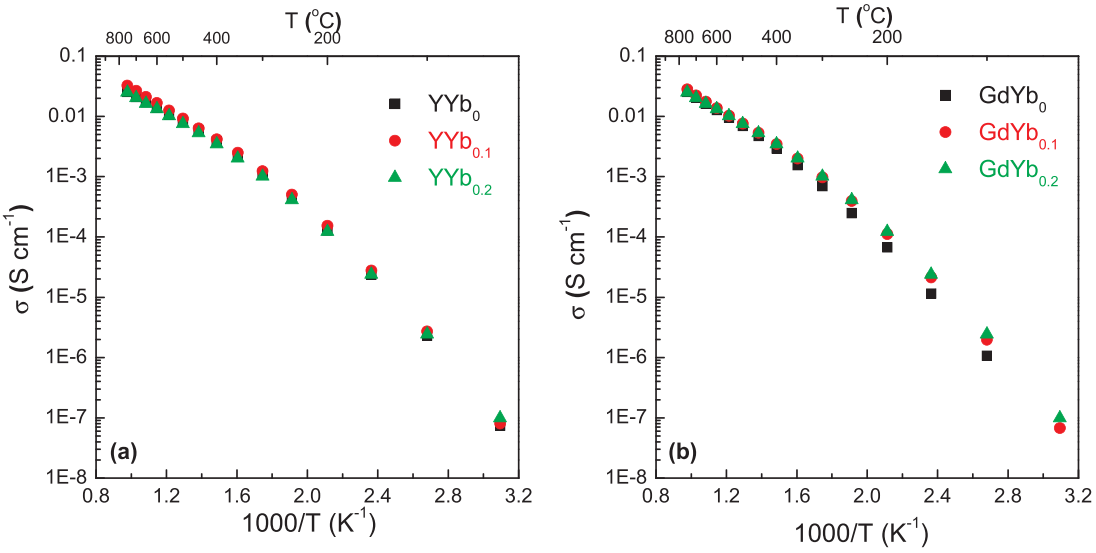

Fig. 9. Arrhenius plots of the overall conductivity of a) $BaCe_{0.6}Zr_{0.2}Y_{0.2-x}Yb_xO_{3-\delta}$ and b) $BaCe_{0.6}Zr_{0.2}Gd_{0.2-x}Yb_xO_{3-\delta}$ series sintered at 1200 °C for 5 h with Zn as sintering aid.

Table 1
Conductivity values in dry and wet air for $BaCe_{0.6}Zr_{0.2}Y_{0.2-x}Yb_xO_{3-\delta}$ and $BaCe_{0.6}Zr_{0.2}Gd_{0.2-x}Yb_xO_{3-\delta}$ (x = 0, 0.05, 0.10, 0.15 and 0.20) with 4 mol% of Zn heated at 1200 °C for 5 h at 750 and 400 °C.

Yb content (x)	$\sigma_{750°C}$ (mS cm^{-1}) dry air	$\sigma_{750°C}$ (mS cm^{-1}) wet air	$\sigma_{400°C}$ (mS cm^{-1}) dry air	$\sigma_{400°C}$ (mS cm^{-1}) wet air
$BaCe_{0.6}Zr_{0.2}Y_{0.2-x}Yb_xO_{3-\delta}$				
0	26	26	1.8	4.0
0.05	30	31	1.7	4.0
0.10	49	33	1.9	4.2
0.15	27	27	1.4	3.2
0.20	25	25	1.5	3.5
$BaCe_{0.6}Zr_{0.2}Gd_{0.2-x}Yb_xO_{3-\delta}$				
0	19	20	1.1	2.3
0.05	18	19	1.0	2.8
0.10	32	28	1.2	3.5
0.15	23	24	1.4	3.0
0.20	25	25	1.5	3.5

boundary resistance of the electrolytes, and the electrode processes are discernible (Fig. 8). The data were fitted with the equivalent circuit of the inset Fig. 8a. The capacitances take the expected values for each contribution ~ pF cm^{-1}, ~ nF cm^{-1} and ~ mF cm^{-1}, for the bulk, grain boundary and electrode response, respectively [28].

Overall conductivities are plotted in Fig. 9 and in Table 1 for both series, where the lowest values are observed for the parent compounds. In general, Yb-containing samples exhibit improved conductivity, and the highest values of conductivity are observed for the intermediate composition of each series x = 0.1, i.e. 33 and 28 mS cm^{-1} at 750 °C for $YYb_{0.10}$ and $GdYb_{0.10}$, respectively. This trend is similar to that reported previously by Yang et al. [22], where the maximum conductivity value for $BaCe_{0.7}Zr_{0.1}Y_{0.2-x}Yb_xO_{3-\delta}$ series is for x = 0.1, 60 mS cm^{-1} at 750 °C. [22]. However, the values are higher than those obtained for $BaCe_{0.6}Zr_{0.3}Y_{0.1}O_{3-\delta}$, about 17 mS cm^{-1} [32]. The different conductivities are due to the different Zr-content. It is worth mentioning that at high temperatures, 750 °C, for both series, the conductivities in dry air are higher than those in wet air, due to a p-type electronic contribution to the overall conductivity [31]. At lower temperatures, 400 °C, the proton conductivity is clearly dominant and all the values in wet atmospheres are higher than in a dry one, where the highest values of conductivity are again observed for the intermediate composition of each series x = 0.1, i.e. 4.2 and 3.5 mS cm^{-1} for $YYb_{0.10}$ and $GdYb_{0.10}$, respectively, lower than the value reported for $BaCe_{0.7}Zr_{0.1}Y_{0.1}Yb_{0.1}O_{3-\delta}$ by Yang et al. [22], 6 mS cm^{-1}.

In order to evaluate the influence of the phase composition and microstructure on the electrical properties, bulk and grain boundary processes were studied separately. In general, bulk conductivity in perovskites depends on the nature of the dopant and its content, since both factors alter the degree of lattice distortion and the free volume for the ionic conduction. $GdYb_x$ samples present somewhat lower values of bulk conductivity than those of YYb_x series (Fig. 8). These differences cannot be only explained by the lattice distortion, since all materials containing Zn crystallize with a cubic structure. Moreover, the samples with Gd-doping exhibit large unit cell volume and consequently larger free volume for ionic conduction. Hence, the different level of dopant segregation into $BaLn_2ZnO_5$ in both series could explain the difference in bulk conductivity.

The specific grain boundary conductivity was estimated to take into consideration the differences in average grain size and composition at the grain boundary region. This was obtained from the relaxation frequency f_{gb} of the grain boundary contribution [20,32]:

$$\sigma_{gb} = 2\pi f_{gb}\,\varepsilon_0\varepsilon_r$$

where ε_o and ε_r are the vacuum and relative permittivity of the sample, respectively, the latter is assumed to be 40 for all compositions [48]. The relaxation frequency of the grain boundary contribution f_{gb} is obtained from the following relation:

$$f_{gb} = \frac{1}{2\pi R_{gb} C_{gb}}$$

where R_{gb} and C_{gb} are the resistance and capacitance, respectively, of the grain boundary contribution.

As expected, the grain boundary conductivity for both series of compounds is one order of magnitude inferior to that of the bulk (Fig. 10). The lowest grain boundary conductivity is observed for $GdYb_0$ and YYb_0. An increase of the Yb-doping results in a slight increase of the conductivity, especially for the GdYb series (Fig. 10b).

The activation energy of the bulk conductivity is practically constant for all compositions, about 0.60 eV, in the temperature range of 50–200 °C. The grain boundary conduction has somewhat higher values of activation energy ~ 0.72 eV. Similar values were reported previously for related compositions.

Therefore, it can be said that Yb-doping leads at low temperatures to a slight increase of the grain boundary conductivity, whereas the bulk

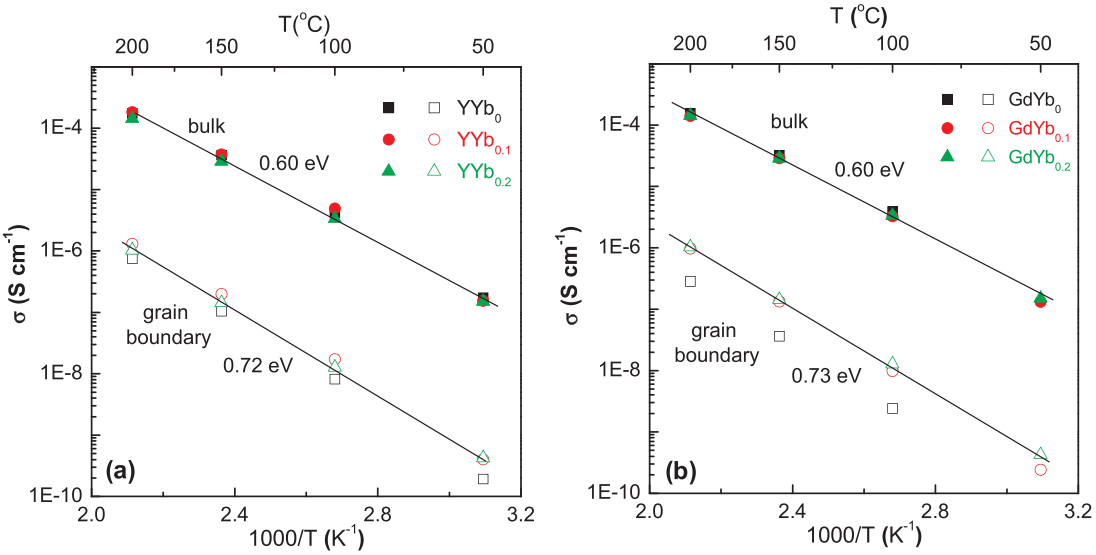

Fig. 10. Arrhenius plots of the bulk and specific grain boundary conductivity of a) $BaCe_{0.6}Zr_{0.2}Y_{0.2-x}Yb_xO_{3-\delta}$ and b) $BaCe_{0.6}Zr_{0.2}Gd_{0.2-x}Yb_xO_{3-\delta}$ series sintered at 1200 °C for 5 h with Zn as sintering aid.

conductivity practically remains unaltered. On the other hand, since Yb-doped BCZ materials showed an enhanced stability towards CO_2, a further characterization in real PC-SOC conditions and under CO_2 atmosphere will be carried out. Finally, the effect of the reaction product $BaLn_2ZnO_4$, which has been identified for the first time in this work, on the stability of these materials needs to be further studied.

4. Conclusions

$BaCe_{0.6}Zr_{0.2}Y_{0.2-x}Yb_xO_{3-\delta}$ and $BaCe_{0.6}Zr_{0.2}Gd_{0.2-x}Yb_xO_{3-\delta}$ (x = 0–0.2) materials were prepared by the freeze-drying method at a reduced temperature of 1200 °C, compared to 1500 °C for the same samples prepared by reactive sintering. The addition of a 4mol% of Zn $(NO_3)_2{\cdot}6H_2O$ led to a decrease of the temperature for both phase formation and densification at 1200 °C. Moreover, Zn addition increase the symmetry of the samples and all compound exhibit a cubic structure, which was confirmed by TEM studies. However, the addition of Zn results in the formation of a secondary phase with composition $BaLn_2ZnO_4$ (Ln=Y, Gd, Yb), which was quantified by the Rietveld method (2–4 wt%), indicating that Zn is segregated into this compound instead of incorporated into the bulk materials. These results indicate that further work is needed to optimize the amount of Zn addition, sintering temperatures and dwelling times, in order to achieve dense ceramic samples without the segregation of $BaLn_2ZnO_5$. The effect of this secondary phase on the electronic conductivity and phase stability of the materials in redox cycles should also be investigated. In addition, TEM studies confirmed the absence of secondary phases at the grain boundary region.

Thermogravimetric analysis showed an increase in the water content uptake as Yb-doping increases. Electrical conductivity was determined by impedance spectroscopy and the highest values are found for x = 0.1 in agreement to previous studies. Equivalent circuit analysis of the impedance spectra revealed that Yb-doping leads to a slight decrease of the grain boundary resistance to the overall conductivity at low temperatures, without altering significantly the bulk contribution.

Acknowledgments

This work was supported by MINECO (Ministerio de Economía y Competitividad) through the MAT2016-77648-R research grant (Spain). J.M.P.-V. thanks the University of Málaga for his funding and Young Researcher project. L. dos Santos-Gomez thanks to the Spanish Ministry of Education, Culture and Sports for her FPU grant (FPU13/03030).

Appendix A. Supplementary material

Supplementary data associated with this article can be found in the online version at http://dx.doi.org/10.1016/j.ceramint.2018.05.010.

References

[1] H. Iwahara, H. Uchida, K. Ono, K.J. Ogaki, Proton conduction in sintered oxides based on $BaCeO_3$, J. Electrochem. Soc. 135 (1988) 529–533.
[2] H. Iwahara, T. Yajima, H. Ushida, Effect of ionic-radii of dopants on mixed ionic-conduction (H^+ + O^{2-}) in $BaCeO_3$-based electrolytes, Solid State Ion. 70 (1994) 267–271.
[3] D. Shima, S.M. Haile, The influence of cation non-stoichiometry on the properties of undoped and gadolinia-doped barium cerate, Solid State Ion. 97 (1997) 443–455.
[4] K. Katahira, Y. Kohchi, T. Shimura, H. Iwahara, Protonic conduction in Zr-substituted $BaCeO_3$, Solid State Ion. 138 (2000) 91–98.
[5] K.H. Ryu, S.M. Haile, Chemical stability and proton conductivity of doped $BaCeO_3$-$BaZrO_3$ solid solutions, Solid State Ion. 125 (1999) 355–367.
[6] N. Zakowsky, S. Williamson, J.T.S. Irvine, Elaboration of CO_2 tolerance limits of $BaCe_{0.9}Y_{0.1}O_{3-\delta}$ electrolytes for fuel cells and other applications, Solid State Ion. 176 (2005) 3019–3026.
[7] N. Osman, I.A. Talib, H.A. Hamid, A.M. Jani, Characterization, electrical conduction and stability of Yb-doped barium cerate prepared by sol–gel method, Ionics 14 (2008) 407–413.
[8] C. Chen, G. Ma, Proton conduction in $BaCe_{1-x}Gd_xO_{3-\alpha}$ at intermediate temperature and its application to synthesis of ammonia at atmospheric pressure, J. Alloy. Compd. 485 (2009) 69–72.
[9] W.B. Wang, J.W. Liu, Y.D. Li, H.T. Wang, F. Zhang, G.L. Ma, Microstructures and proton conduction behaviors of Dy-doped $BaCeO_3$ ceramics at intermediate temperature, Solid State Ion. 181 (2010) 667–671.
[10] M. Oishi, S. Akoshima, K. Yashiro, K. Sato, T. Kawada, J. Mizusaki, Defect structure analysis of proton-oxide ion mixed conductor $BaCe_{0.9}Nd_{0.1}O_{3-\delta}$, Solid State Ion. 181 (2010) 1336–1343.
[11] R. Muccillo, E.N.S. Muccillo, Synthesis and properties of $BaZr_{0.1}Ce_{0.7}Y_{0.2-x}M_xO_{3-\delta}$ (x = 0, 0.1; M = Dy, Yb) compounds, ECS Trans. 35 (2011) 1251–1258.
[12] Y. Liu, Y. Guo, R. Ran, Z. Shao, A new neodymium-doped $BaZr_{0.8}Y_{0.2}O_{3-\delta}$ as potential electrolyte for proton-conducting solid oxide fuel cells, J. Membr. Sci. 415–416 (2012) 391–398.
[13] Q.A. Islam, S. Nag, R.N. Basu, Electrical properties of Tb-doped barium cerate, Ceram. Int. 39 (2013) 6433–6440.
[14] Y.-J. Gu, Z.-G. Liu, J.-H. Ouyang, F.-Y. Yan, Y. Zhou, Structure and electrical conductivity of $BaCe_{0.85}Ln_{0.15}O_{3-\delta}$ (Ln = Gd, Y, Yb) ceramics, Electrochim. Acta 105 (2013) 547–553.
[15] R. Kannan, S. Gill, N. Maffei, V. Thangadurai, $BaCe_{0.85-x}Zr_xSm_{0.15}O_{3-\delta}$ (0.01 < x < 0.3) (BCZS): effect of Zr content in BCZS on chemical stability in CO_2 and H_2O vapor, and proton conductivity, J. Electrochem. Soc. 160 (2013) F18–F26.
[16] J. Bu, P.G. Jönsson, Z. Zhao, Ionic conductivity of dense $BaZr_{0.5}Ce_{0.3}Ln_{0.2}O_{3-\delta}$ (Ln = Y, Sm, Gd, Dy) electrolytes, J. Power Sources 272 (2014) 786–793.
[17] J. Song, B. Meng, X. Tan, Stability and electrical conductivity of

$BaCe_{0.85}Tb_{0.05}M_{0.1}O_{3-\delta}$ (M = Co, Fe, Y, Zr, Mn) high temperature proton conductors, Ceram. Int. 42 (2016) 13278–13284.
[18] J. Lyagaeva, N. Danilov, G. Vdovin, J. Bu, D. Medvedev, A. Demina, P. Tsiakaras, A new Dy-doped $BaCeO_3$–$BaZrO_3$ proton conducting material as a promising electrolyte for reversible solid oxide fuel cells, J. Mater. Chem. A 4 (2016) 15390–15399.
[19] N. Danilov, E. Pikalova, J. Lyagaeva, B. Antonov, D. Medvedev, A. Demin, P. Tsiakaras, J. Power Sources 366 (2017) 161–168.
[20] M. Amsif, D. Marrero-Lopez, J.C. Ruiz-Morales, S.N. Savvin, M. Gabás, P. Núñez, Influence of rare-earth doping on the microstructure and conductivity of $BaCe_{0.9}Ln_{0.1}O_{3-\delta}$ proton conductors, J. Power Sources 196 (2011) 3461–3469.
[21] N. Bonanos, B. Ellis, K.S. Knight, M.N. Mahmood, Ionic conductivity of gadolinium-doped barium cerate perovskites, Solid State Ion. 35 (1989) 179–188.
[22] L. Yang, S. Wang, K. Blinn, M. Liu, Z. Liu, Z. Cheng, M. Liu, Enhanced sulfur and coking tolerance of a mixed ion conductor for SOFCs: $BaZr_{0.1}Ce_{0.7}Y_{0.2-x}Yb_xO_{3-\delta}$, Science 326 (2009) 126–129.
[23] H. Ding, X. Xue, $BaZr_{0.1}Ce_{0.7}Y_{0.1}Yb_{0.1}O_{3-\delta}$ electrolyte-based solid oxide fuel cells with cobalt-free $PrBaFe_2O_{5+\delta}$ layered perovskite cathode, J. Power Sources 195 (2010) 7038–7041.
[24] S. Wang, F. Zhao, L. Zhang, F. Chen, Synthesis of $BaCe_{.7}Zr_{0.1}Y_{0.1}Yb_{0.1}O_{3-\delta}$ proton conducting ceramic by a modified Pechini method, Solid State Ion. 213 (2012) 29–35.
[25] N.T.Q. Nguyen, H.H. Yoon, Preparation and evaluation of $BaZr_{0.1}Ce_{0.7}Y_{0.1}Yb_{0.1}O_{3-\delta}$ (BZCYYb) electrolyte and BZCYYb-based solid oxide fuel cells, J. Power Sources 231 (2013) 213–218.
[26] T. Jiang, Y. Liu, Z. Wang, W. Sun, J. Qiao, K. Sun, An improved direct current sintering technique for proton conductor - $BaZr_{0.1}Ce_{0.7}Y_{0.1}Yb_{0.1}O_3$: the effect of direct current on sintering process, J. Power Sources 248 (2014) 70–76.
[27] H. Sun, S. Zhang, C. Li, B. Rainwater, Y. Liu, L. Zhang, Y. Zhang, C. Li, M. Liu, Atmospheric plasma-sprayed $BaZr_{0.1}Ce_{0.7}Y_{0.1}Yb_{0.1}O_{3-\delta}$ (BZCYYb) electrolyte membranes for intermediate-temperature solid oxide fuel cells, Ceram. Int. 42 (2016) 19231–19236.
[28] M. Amsif, D. Marrero-López, A. Magrasó, J. Pena-Martínez, J.C. Ruiz-Morales, P. Núñez, Synthesis and characterisation of $BaCeO_3$-based proton conductors obtained from freeze-dried precursors, J. Eur. Ceram. Soc. 29 (2009) 131–138.
[29] E. Gorbova, V. Maragou, D. Medvedev, A. Demin, P. Tsiakaras, Influence of sintering additives of transition metals on the properties of gadolinium-doped barium cerate, Solid State Ion. 179 (2008) 887–890.
[30] S. Nikodemski, J. Tong, C. Duan, R. O'Hayre, Ionic transport modification in proton conducting $BaCe_{0.6}Zr_{0.3}Y_{0.1}O_{3-\delta}$ with transition metal oxide dopants, Solid State Ion. 294 (2016) 37–42.
[31] M. Amsif, D. Marrero-López, J.C. Ruiz-Morales, S.N. Savvin, P. Núñez, Effect of sintering aids on the conductivity of $BaCe_{0.9}Ln_{0.1}O_{3-\delta}$, J. Power Sources 196 (2011) 9154–9163.
[32] M. Amsif, D. Marrero-López, J.C. Ruiz-Morales, S.N. Savvin, P. Núñez, The effect of Zn addition on the structure and transport properties of $BaCe_{0.9-x}Zr_xY_{0.1}O_{3-\delta}$, J. Eur. Ceram. Soc. 34 (2014) 1553–1562.
[33] S. Tao, J.T.S. Irvine, A stable, easily sintered proton-conducting oxide electrolyte for moderate-temperature fuel cells and electrolyzers, Adv. Mater. 18 (2006) 1581–1584.
[34] S. Tao, J.T.S. Irvine, Conductivity studies of dense yttrium-doped $BaZrO_3$ sintered at 1325 °C, J. Solid State Chem. 180 (2007) 3493–3503.
[35] P. Babilo, S.M. Haile, Enhanced sintering of yttrium-doped barium zirconate by addition of ZnO, J. Am. Ceram. Soc. 88 (2005) 2362–2368.
[36] H. Wang, R. Peng, X. Wu, J. Hu, C. Xia, Sintering behavior and conductivity study of yttrium-doped $BaCeO_3$–$BaZrO_3$ solid solutions using ZnO additives, J. Am. Ceram. Soc. 92 (2009) 2623–2629.
[37] X'Pert HighScore Plus Software, v3.0e, PANalytical B. V., Amelo, The Netherlands, 2012.
[38] A.C. Larson, R.B.V. Dreele, General Structure Analysis System (GSAS) Software, Los Alamos National Lab, Rep. No.LA-UR-86748.
[39] J.C.C. Abrantes, Estereologia, UIDM, ESTG; Polytechnic Institute of Viana do Castelo: Viana do Castelo, Portugal, 1998.
[40] D. Johnson, ZView, A Software Program for IES Analysis, Version 2.8, Scribner Associates, Inc., Southern Pines, NC, 2002.
[41] Z. Shin, W.P. Sun, W. Liu, Synthesis and characterization of $BaZr_{0.3}Ce_{0.5}Y_{0.2-x}Yb_xO_{3-\delta}$ proton conductor for solid oxide fuel cells, J. Power Sources 245 (2014) 953–957.
[42] L. Malavasi, C. Tealdi, C. Ritter, V. Pomjakushin, F. Gozzo, Y. Diaz-Fernandez, Combined neutron and synchrotron X-ray diffraction investigation of the $BaCe_{0.85-x}Zr_xY_{0.15}O_{3-\delta}$ ($0.1 < x < 0.4$) proton conductors, Chem. Mater. 23 (2011) 1323–1330.
[43] J. Lyagaeva, G. Vdovin, L. Hakimova, D. Medvedev, A. Demina, P. Tsiakaras, $BaCe_{0.5}Zr_{0.3}Y_{0.2-x}Yb_xO_{3-\delta}$ proton-conducting electrolytes for intermediate-temperature solid oxide fuel cells, Electrochim. Acta 251 (2017) 554–561.
[44] Z. Sun, E. Fabbri, L. Bia, E. Traversa, Lowering grain boundary resistance of $BaZr_{0.8}Y_{0.2}O_{3-\delta}$ with $LiNO_3$ sintering-aid improves proton conductivity for fuel cell operation, Phys. Chem. Chem. Phys. 13 (2011) 7692–7700.
[45] J.-S. Park, J.-H. Lee, H.-W. Lee, B.-K. Kim, Low temperature sintering of $BaZrO_3$-based proton conductors for intermediate temperature solid oxide fuel cells, Solid State Ion. 181 (2010) 163–167.
[46] Q. Dong, Z.H. Dub, T.S. Zhang, J. Lu, X.C. Song, J. Ma, Sintering and ionic conductivity of 8YSZ and CGO10 electrolytes with small addition of Fe_2O_3: a comparative study, Int. J. Hydrog. Energy 34 (2009) 7903–7909.
[47] H.P. Wang, L.J. Zhang, X.M. Liu, H.L. Bi, S.L. Yu, F. Han, L. Pei, Electrochemical study on $Ce_{0.85}Sm_{0.15}O_{1.925}$-$BaCe_{0.83}Y_{0.17}O_{3-\delta}$ composite electrolyte, J. Alloy. Compd. 632 (2015) 686–694.
[48] P. Babilo, T. Uda, S.M. Haile, Processing of yttrium-doped barium zirconate for high proton conductivity, J. Mater. Res. 22 (2007) 1322–1330.